

Microscopic structure of electromagnetic whistler wave damping by kinetic mechanisms in hot magnetized Vlasov plasmas

Anjan Paul^{1,2} and Devendra Sharma^{1,2}

¹*Institute for Plasma Research, Bhat, Gandhinagar, India, 382428*

²*Homi Bhabha National Institute, Training School Complex, Anushaktinagar, Mumbai 400094, India*

(Dated: October 26, 2022)

The kinetic damping mechanism of low frequency transverse perturbations propagating parallel to the magnetic field in a magnetized warm electron plasma is simulated by means of electromagnetic (EM) Vlasov simulations. The short-time-scale damping of the electron magnetohydrodynamic whistler perturbations and underlying physics of finite electron temperature effect on its real frequency are recovered rather deterministically, and analyzed. The damping arises from an interplay between a global (prevailing over entire phase-space) and the more familiar resonant-electron-specific kinetic damping mechanisms, both of which preserve entropy but operate distinctly by leaving their characteristic signatures on an initially coherent finite amplitude modification of the warm electron equilibrium distribution. The net damping results from a *deterministic* thermalization, or *phase-mixing* process, largely supplementing the resonant acceleration of electrons at shorter time scales, relevant to short-lived turbulent EM fluctuations. A kinetic model for the evolving initial transverse EM perturbation is presented and applied to signatures of the whistler wave phase-mixing process in simulations.

I. INTRODUCTION

The electromagnetic turbulence prevails in collective excitations of charged matter interacting with, and by means of, the electromagnetic field over a vast range of spatiotemporal scales, usually terminated by dissipation at the finer scales. The solar-wind spectrum, for example, shows that beyond a frequency *breakpoint* a deviation exists from the inertial range characterized by exponent $-5/3$ of power law [1, 2]. In one of the plausible scenarios, the whistler fluctuations can be the fundamental mode and central means of dissipation in this weak turbulence regime [3]. A steepening present in the spectrum leading to considerably high spectral exponents ($\sim 2-3$) suggests presence of considerable damping alongside to the intra-spectral energy transfer [3]. Besides by conversion to electrostatic modes [4], damping by kinetic transverse wave-particle interaction must operate on the short lived excitations [5–8] initiated by spontaneous field fluctuations. Fresh perturbations, so triggered, excite warm plasma eigenmodes by leaving long lasting remnants of their initially enforced phase-space structure in the memory of nonthermal kinetic distributions [9]. The asymptotic long-time solutions of the collisionless kinetic formulation [10, 11] applied to them therefore have large scope of sophistication by admitting a strong *deterministic thermalization*, or phase-mixing [9], alongside the damping evaluated in usual time asymptotic, $t \rightarrow 0$ limit.

The general kinetic evolution produced collisionless damping of electromagnetic fluctuations [12] involves a rather complicated phase-space dynamics and is most accessible by deterministic Vlasov simulations [13, 14]. Only a limited number of studies have rather deterministically simulated the dynamics of the transverse electromagnetic excitations and their damping/stability in a hot collisionless magnetized plasma [15, 16], even as the process remains critical for determining the operational

state of turbulence and the transport associated with it both in space plasmas [3, 17] as well as in modern magnetic confinement fusion experiments [18].

In the collisionless limit, the modifications made to temperature, or width, of an initially equilibrium warm electron velocity distribution produce a higher order correction to the resonant wave particle interaction process. The analytical model predicts a related downward shift in the whistler wave frequency in collisionless plasmas with hotter electrons [8, 19, 20]. The recovered strength of damping due to wave particle interaction however remains underestimated in comparison with that produced by the computer simulations implemented with reasonably low collisionality.

This paper addresses above aspects of kinetic whistler damping mechanism, subsequent to the recovery of general electromagnetic modes of a magnetized plasma and their dispersive characterization in our flux-balance based [13, 21] Vlasov simulations. This is accompanied by illustration of its detailed *phase-spatiotemporal* evolution. The interaction of electromagnetic modes, propagating parallel to the magnetic field with the resonant particles is studied, particularly recovering the damping of the whistler waves via full kinetic mechanism and comparison of the simulation results with those analytically prescribed in the linear Landau theory limit [9, 10]. Presented simulations and analysis enter the finer regime of kinetic phase-mixing of the electromagnetic mode uniquely achievable by Vlasov simulations. We qualitatively recover the phase-mixing effects showing the dominance of frequency $\mathbf{v} \cdot \mathbf{k}$ of the ballistic term ($\propto \exp(ikvt)$) [9] accounting for short time response, in addition to time asymptotic Landau damping results that are routinely applied to turbulent electromagnetic fluctuations of sufficiently short life time. First quantitative analysis of the *phase-spatiotemporal* evolution of a 4D electron phase-space distribution perturbation associated

with the transverse electromagnetic whistler mode simulated in a hot magnetized Vlasov plasma is presented.

The present paper is organized as follows. In Sec. II the electromagnetic Vlasov-Maxwell model considered for the simulation is presented. Vlasov simulation implementation and its characterization by dispersion of transverse EM perturbation is presented in Sec. III. In Sec. IV the simulations of Landau damping of transverse whistler wave perturbations in a warm electron plasma is presented followed by their comparison with analytical results. Based on the evolution of simulated perturbations, the signatures of phase-mixing supplemented Landau damping of the initial perturbation are presented in Sec. V. The kinetic model for initial transverse EM perturbations is presented and solved in Sec. VB. Conclusions are presented in Sec. VI.

II. THE ELECTROMAGNETIC VLASOV PLASMA MODEL

The electromagnetic magnetized plasma modes simulated in this paper follow pure kinetic formulation and are well represented by the solutions of collisionless, fully nonlinear Vlasov equation for species α ,

$$\frac{\partial f_\alpha}{\partial t} + \mathbf{v} \cdot \frac{\partial f_\alpha}{\partial \mathbf{x}} + \frac{q_\alpha}{m_\alpha} \left(\mathbf{E} + \frac{\mathbf{v} \times \mathbf{B}}{c} \right) \frac{\partial f_\alpha}{\partial \mathbf{v}} = 0. \quad (1)$$

The evolution of electric field \mathbf{E} and magnetic field \mathbf{B} for the electromagnetic processes follows the Maxwell's equations,

$$\nabla \times \mathbf{B} = \frac{1}{c} \frac{\partial \mathbf{E}}{\partial t} + \frac{4\pi}{c} \mathbf{J}, \quad (2)$$

$$\nabla \times \mathbf{E} = -\frac{1}{c} \frac{\partial \mathbf{B}}{\partial t}, \quad (3)$$

$$\nabla \cdot \mathbf{B} = 0 \quad (4)$$

where the current density \mathbf{J} is described by

$$\mathbf{J} = \sum_\alpha \int_{-\infty}^{\infty} d\mathbf{v} q_\alpha \mathbf{v} f_\alpha \quad (5)$$

Consistent with the electron magnetohydrodynamic regime excitations, we use an externally applied constant magnetic field \mathbf{B}_0 and infinitely massive ions. The subscript for species α therefore only assumes value, e , representing electrons (and henceforth omitted), which are the only mobile species and contributing to the perturbation.

The full nonlinear kinetic model (1)-(5) is implemented for the case of waves propagating parallel to an applied magnetic field ($\mathbf{B}_0 \parallel \mathbf{k}$) where principle modes are high and low frequency right and left handed circularly polarized modes. This set up includes the whistler waves that are right handed polarized and propagate in the frequency range $\Omega_{ci} < \omega < \Omega_{ce}$, where $\Omega_{c\alpha}$ is the gyrofrequency of the species α .

III. KINETIC SIMULATIONS OF ELECTROMAGNETIC WAVES IN MAGNETIZED WARM VLASOV PLASMA

The simulations presented in this analysis progress by numerically evolving the magnetized plasma (electron) velocity distribution function f according to the dynamics of the phase-fluid flow [9] which is governed by the collisionless Vlasov equation (1), and associated Maxwell's equations (2)-(4). The 4-dimensional (4D \equiv 1x-3v) phase-space simulations are performed using an advanced flux balance technique [13, 21, 22] generalized to simulate the electromagnetic plasma modes in a large range of magnetization of plasma species. The results of simulations are characterized first against the analytical dispersion relation of left and right handed circularly polarized low and high frequency modes and then against both analytic and numerical evaluation of the linear Landau damping descriptions [8, 9, 23].

A. The simulation set-up

In order to simulate the waves propagating parallel to an ambient magnetic field \mathbf{B}_0 in a wide range of frequency ω and wave vector \mathbf{k} , we have assumed a setup where both the \mathbf{B}_0 and \mathbf{k} are aligned to z -axis and the periodic boundary condition is used at both the boundaries of the one-dimensional simulation zone located between $z = 0$ and L . The setup therefore assumes symmetry along both \hat{x} and \hat{y} directions with finite spread of electron velocities along these dimensions, besides the direction \hat{z} . The three dimensional equilibrium velocity distribution for the electron species is considered to be a Maxwellian,

$$f(z, \mathbf{v}) = \left(\frac{1}{2\pi v_{th}^2} \right)^{3/2} \prod_{j=x,y,z} \exp \left\{ -\frac{(v_j - \langle v_j \rangle)^2}{2v_{th}^2} \right\}, \quad (6)$$

where $v_{th} = (T_e/m_e)^{1/2}$ is electron thermal velocity, T_e is electron temperature in energy units and m_e is electron mass.

At time $t = 0$, the equilibrium distribution is perturbed with sinusoidal perturbations (having variation along \hat{z}) with initial amplitudes of $\langle \mathbf{v} \rangle_1$, \mathbf{E}_1 and \mathbf{B}_1 ($\propto \exp(ikz)$) consistent with transverse electromagnetic (right or left handed circularly polarized) linear magnetized plasma modes propagating with a desired k [5, 24].

B. Dispersion characterization of electromagnetic plasma modes

We present the dispersion relations recovered for the case of very small electron thermal velocity ($v_{th} = 0.001 c$) simulated and its comparison with the corresponding analytical cold plasma dispersion relation [24, 25]. Specific to simulation cases presented in this section, we have

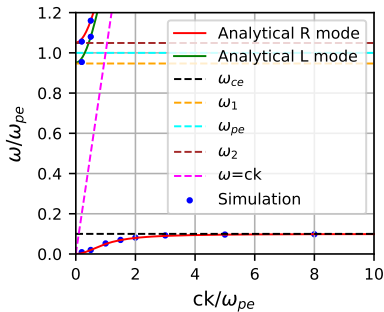


FIG. 1. Dispersion of simulated frequency (dots) compared to the Right and Left handed polarized branches of the analytical dispersion relation (solid line).

used a 3-dimensional velocity space grid of rather moderate size having $32 \times 32 \times 32$ grid points, in combination with spatial grid size also of 32 grid points. In Fig. 1, the comparison is presented of the simulated values of frequency ω of the perturbation plotted as function of k , with the right and left handed circularly polarized (RHCP and LHCP) branches of the analytical dispersion relation in the limit of infinitely massive ions ($\omega_{pe} \gg \omega_{pi}$),

$$k_{R,L}^2 = \frac{\omega^2}{c^2} \left[1 - \frac{\omega_{pe}^2}{\omega(\omega \mp \Omega_{ce})} \right]. \quad (7)$$

Considering the parameters, $v_{th} = 0.001 c$, the ratio of electron cyclotron frequency and plasma frequency $\Omega_{ce}/\omega_{pe} = 0.1$ and sufficiently small initial perturbation exclusively in electron average velocity amplitude $\Delta V = \langle v \rangle_{1\max} - \langle v \rangle_{1\min} = 2 \times 10^{-3}c$, the high frequency ($\omega > \Omega_{ce}$) RHCP and LHCP mode phase velocities are sufficiently high for these waves to stay out of resonance with the cold electrons chosen for this case. Moreover, for the low frequency whistler waves excited (dots on the red curve in the region $0 < \omega < \Omega_{ce}$ in Fig. 1), the electron thermal velocity $v_{th} = 0.001c$ chosen is still sufficiently low for no significant resonant electron population to be available at the resonant velocity, $v_z = v_{res} = (\omega - \Omega_{ce})/k$. In rest of this analysis we exclusively characterize this low frequency whistler branch of the perturbation for relatively warmer electrons in order to analyze its resonant damping.

IV. LANDAU DAMPING OF THE TRANSVERSE WHISTLER MODE

An advanced simulation set up, with grid size of $64 \times 64 \times 64 \times 64$ is implemented in the following sets of simulations, by adopting the electron velocity range $[-0.26, 0.26] c$. The velocity distribution of electrons as function of the parallel velocity $v_{\parallel} \equiv v_z$ is plotted in Fig. 2 at $v_x = v_y = 0$ for a range of electron thermal velocity $v_{th} = 0.001c$ (inner most profile) to $0.026c$ (outer

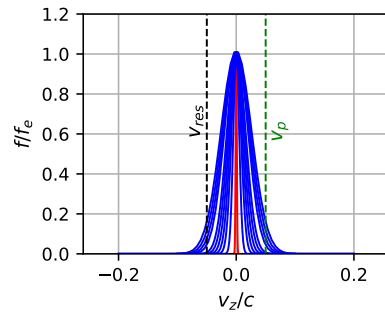


FIG. 2. The electron distribution function (normalized to its maximum value) plotted as function of parallel velocity $v_{\parallel} \equiv v_z$ at $v_x = v_y = 0$. The thermal velocity of electrons for the curves with increasing width ranges from $v_{th} = 0.001c$ (inner most profile) to $0.026c$ (outer most profile), respectively. The vertical dotted lines indicate resonant velocity v_{res} and phase velocity v_p of the low frequency whistler mode at $k = 1.0\omega_p/c$.

most profile) explored in the cases presented in this section. The resonant velocity $v_{res} = (\omega - \Omega_{ce})/k$ and phase velocity v_p of the low frequency whistler mode for parameters $k = 1.0\omega_p/c$ and $\Omega_{ce}/\omega_p = 0.1$, are indicated by vertical dotted line. The profiles for smaller values of v_{th} show the population of resonant electrons drops to negligible values such that no resonant damping is present for these cases.

In Fig. 3(a), the time evolution of the amplitude of the velocity perturbation ΔV is plotted in the simulations done for the range of electron thermal velocity $v_{th} = 0.001c$ to $0.026c$ for the value of $k = 0.8\omega_{pe}/c$. Two additional set of simulations done for the values of $k = 0.897$ and $k = 1.0\omega_{pe}/c$ are presented in Fig. 3(b) and Fig. 3(c), respectively. The time evolution of ΔV in all the cases above cover the initial evolution of the wave amplitude only for the time duration $\Delta t \sim 3\omega_p^{-1}$ (i.e., about a fraction of one complete cycle of the whistler wave with frequency $\omega < \Omega_{ce}$ while $\Omega_{ce}/\omega_p = 0.1$) which is the time duration in which the linear Landau damping rate remains reasonable estimate for the wave damping. The short time evolution in Fig. 3 has sufficiently low numerical widening of f for resolving the effect of T_e variation, which is varied with relatively much larger increments in this study.

A. Comparison of simulations with analytic whistler damping rates

The damping rates of whistler velocity perturbation amplitude can be compared with the available analytic approximations of the Landau damping rate of whistlers. For the purpose of comparison we have used the analytic results from kinetic formulation in certain limiting cases. The numerical evaluation of analytical expression is done

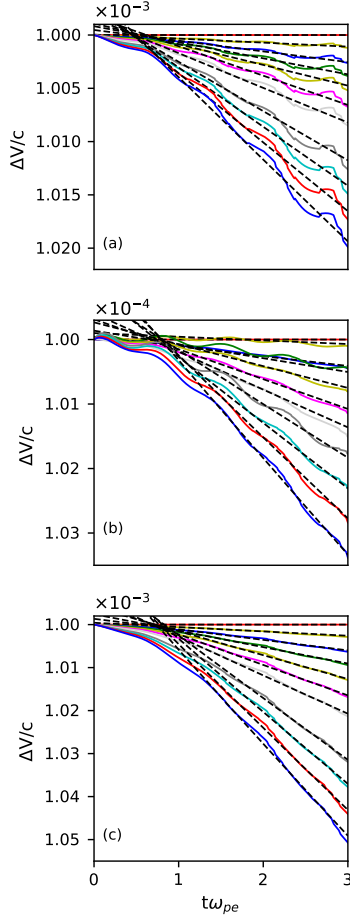


FIG. 3. The decay in the velocity perturbation Δv for $v_{th} = 0.001c$ (lowest damping) to $0.026c$ (highest damping) for (a) $k = 0.8\omega_{pe}/c$, (b) $k = 0.897\omega_{pe}/c$ and (c) $k = 1.0\omega_{pe}/c$. The modulation seen in some cases are residual RHCP and LHCP excitations ($\omega_{R,L} > \Omega_{ce}$ satisfying (18)).

in the limits where such approximations become unavailable. We begin by using the kinetic dispersion relation for the electromagnetic waves ([26] and Sec. VB) given by,

$$c^2k^2 - \omega^2 = \frac{8\pi^2q_e^2}{m} \int_{-\infty}^{\infty} \int_0^{\infty} \frac{[(\omega - kv_z) \frac{\partial f_{e0}}{\partial v_{\perp}} + kv_{\perp} \frac{\partial f_{e0}}{\partial v_z}]}{(\omega - kv_z \pm \Omega_{ce})} \times v_{\perp}^2 dv_{\perp} dv_z. \quad (8)$$

Assuming isotropy in the velocity space,

$$\frac{\partial f_0}{\partial v_{\parallel}} = \frac{\partial f_0}{\partial v_{\perp}}, \quad (9)$$

additionally considering the whistler wave frequency limit $\Omega_{ci} \ll \omega \ll \Omega_{ce}$ and for wavelengths larger than electron gyroradius, $\lambda > \rho_{ce}$, we recover [9],

$$\gamma \approx -\frac{\omega_{pe}^2}{|k_{\parallel}|v_{th}} \frac{1}{1 + k^2c^2/\omega_r^2} \exp\left(-\frac{\Omega_{ce}^2}{k_{\parallel}^2v_{th}^2}\right). \quad (10)$$

However, for the cases explored in the present simulations have $\omega \lesssim \Omega_{ce}$ and the expression (10) underestimates the damping rate γ , yielding negligible values in comparison to what recovered in the simulations. For example, for $k = 1.0\omega_{pe}/c$, $v_{th} = 0.026c$, $\Omega_{ce} = 0.1\omega_{pe}$, $\gamma \sim 10^{-8}\omega_{pe}$, although a considerably higher damping ($\gamma \sim 10^{-3}\omega_{pe}$) is recovered in the simulations. An estimate from (8) in the limit $\omega \lesssim \Omega_{ce}$ more relevant to simulations is prescribed by Gary [23] in the form of a general expression for γ ,

$$\gamma \approx -\frac{\pi}{2k} \sum_{\alpha} \frac{\omega_{p\alpha}^2}{\sqrt{2\pi}v_{th\alpha}} \exp\left(-\frac{(\omega \pm \Omega_{c\alpha})^2}{2k_{\parallel}^2v_{th\alpha}^2}\right) \quad (11)$$

which can be used as an alternate analytic estimate to compare with theory the whistler damping rate recovered in the simulations. For an even improved analytic estimate of damping rates we have also used the exact expression (8) and evaluated γ numerically, by the following procedure.

As in the simulation where ions are infinitely massive, considering electron equilibrium distribution to be Maxwellian,

$$f_0 = \left(\frac{1}{2\pi}\right)^{\frac{3}{2}} \frac{1}{v_{th\parallel e}v_{th\perp e}^2} \exp\left(-\frac{v_{\perp}^2}{2v_{th\perp e}^2} - \frac{v_{\parallel}^2}{2v_{th\parallel e}^2}\right), \quad (12)$$

and substituting it in the dispersion (8), one obtains [8],

$$\omega^2 + \omega_{pe}^2 I - c^2k^2 = 0, \quad (13)$$

where,

$$I = \frac{v_{th\perp e}^2}{v_{th\parallel e}^2} - 1 + \left[\frac{v_{th\perp e}^2}{v_{th\parallel e}^2} \frac{\omega \pm \Omega_{ce}}{\mp \Omega_{ce}} + 1\right] \frac{\mp \Omega_{ce}}{\sqrt{2}kv_{th\parallel e}} Z(\zeta), \quad (14)$$

and $Z(\zeta)$ is the plasma dispersion function [27],

$$Z(\zeta) = \frac{1}{\sqrt{\pi}} \int_{-\infty}^{\infty} \frac{e^{-t^2}}{t - \zeta} dt, \quad (15)$$

with the argument

$$\zeta = \frac{\omega \mp \Omega_{ce}}{\sqrt{2}kv_{th\parallel e}}. \quad (16)$$

The upper and lower sign in Eq. (14) are for RHCP and LHCP waves, respectively. Applying dispersion (13) to whistlers which are right handed polarized, and considering isotropy of the distribution ($v_{th\parallel} = v_{th\perp} = v_{th}$) we get (13) in the form,

$$\omega^2 + \omega \frac{\omega_{pe}^2}{\sqrt{2}kv_{th}} Z(\zeta) - c^2k^2 = 0. \quad (17)$$

Note that under cold plasma approximation where imaginary part of the function $Z(\zeta) = i\sqrt{\pi}e^{-\zeta^2} - \frac{1}{\zeta}$ is negligible

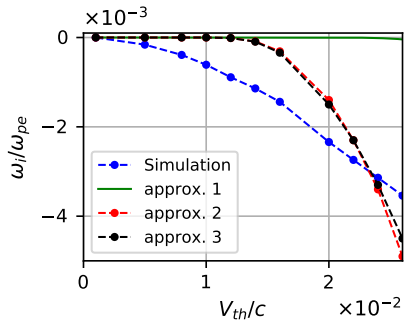


FIG. 4. Comparison of simulated damping rate γ with that obtained from analytical approximations, approx-1 (10), approx-2 (19) and approx-3 (11) done for $k = 1.0\omega_p/c$ or simulation box length $L = 2\pi c/\omega_p$.

and $Z(\zeta) \sim -1/\zeta$, such that with $\zeta = (\omega - \Omega_{ce})/\sqrt{2}kv_{th}$ one readily recovers from (17), the cold plasma dispersion relation for the RHCP waves,

$$\omega^2 - \omega \frac{\omega_{pe}^2}{(\omega - \Omega_{ce})} - c^2 k^2 = 0, \quad (18)$$

which is the whistler dispersion relation in the limit $\Omega_{ci} < \omega < \Omega_{ce}$. Considering $\omega = \omega_r + i\omega_i$, in the warm plasma RHCP dispersion (17) we obtain for $\gamma = \omega_i \ll \omega_r$ [8, 20],

$$\gamma = -\frac{\omega_r \sqrt{\pi} e^{-\zeta^2} \sqrt{2} k v_{th}}{[\omega_r Z'(\zeta) + \sqrt{2} k v_{th} Z(\zeta) + 2\omega_r k^2 v_{th}^2]}, \quad (19)$$

where $Z'(\zeta)$ is the derivative of $Z(\zeta)$ with respect to ζ .

Comparison of the damping rate recovered in simulations with the analytical approximations (10), (11) and (19) is presented in Fig. 4 for the above range of v_{th} values for which simulations are performed using $k = 0.897\omega_p/c$ or simulation box length $L = 7c/\omega_p$. Note that for the nearly cold electron case, $v_{th} \rightarrow 0$, the simulations (blue dots) duly recover a whistler propagation free of any damping (or growth), confirming that the deviation from this undamped propagation recovered at large electron temperature values (larger $v_{th} > 0$) represents pure kinetic effects in the simulations. The simulations however show increasing damping from finite v_{th} values while all the other analytical approximations prescribe comparable damping only beyond $v_{th} > 1.0 \times 10^{-2}c$, as discussed further below.

Suitability of approximation (10) for the present range is ruled out by the negligible resonant damping prescribed by (10) as plotted in Fig. 4 using green line in comparison to other estimates of γ , namely, (11) and (19) plotted with red and black lines, respectively. The analytical approximation (11) very closely estimates the numerically evaluated values of the exact expression (19). We note that despite no clear approximations used in them (at least, in the numerically computed γ from (19)) besides their linear origin, they still show finite discrepancy from the simulated damping rates. In general,

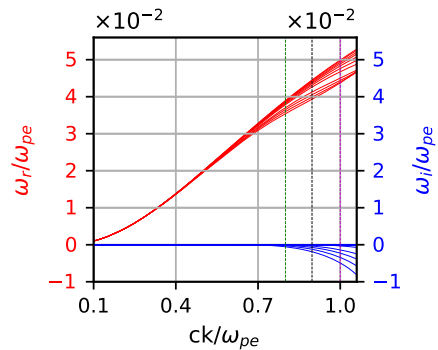


FIG. 5. Simulated frequency and damping rate γ as function of k and a range in electron thermal velocity values $v_{th} = 0.001$ to 0.026 . The vertical dashed lines indicate k values for which sets of simulations are performed by varying v_{th} .

the simulations recover stronger damping rates for the whistlers than what prescribed by the analytical damping rate approximations duly obtained from the kinetic dispersion relation. We explore the origin of this discrepancy for whistlers excitations in Sec. V based on the deterministic evolution of the electron distribution function in essential 4D phase-space set up available from the simulations. The missing physics is located in the small time evolution of the initial perturbations as asymptotic contributions are duly accounting for in estimating the kinetic Landau damping rate. For turbulent situations, where the excited fluctuations are short lived, the short time contributions need to be accounted for. Moreover, they might dominate the asymptotic mechanisms in certain relevant limits.

In Fig. 5 the analytically obtained whistler frequency ω and more accurate numerically computed damping rate from (19) are plotted as function of k for several (> 10) different values of electron thermal velocity in range $v_{th} = 0.001$ to 0.026 . In Fig 6, the ω_r and γ values are separately compared with analytical values where the markers represent simulated data and variation is done in both k and v_{th} values. As in Fig 6, simulations confirm the analytical prediction that the ω_r slightly reduces at larger electron temperature, though the analytical ω_r overestimates this reduction for larger v_{th} . The comparison of γ presented in Fig. 6 shows that while at $k = 0.8\omega_p/c$ the damping rate in simulation is recovered to be stronger than the corresponding analytic values, at larger k values, $0.897\omega_p/c$ and $1\omega_p/c$, the overlap in the analytic and simulated γ values is better, especially at larger v_{th} values. It can also be noted that at smaller k , analytical expressions underestimate of the damping and the spread in kinetic γ values is larger than the analytical value spread. At larger k , on the other hand, the analytical approximation overestimates γ and the kinetically obtained γ values have a narrower spread.

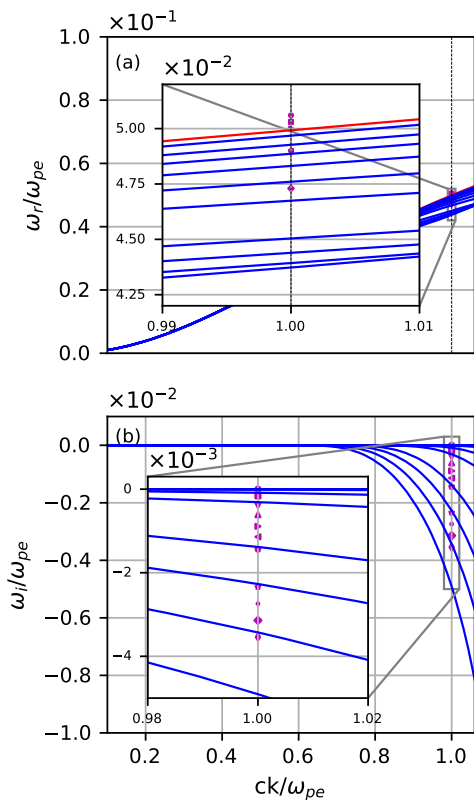


FIG. 6. Comparison of simulated frequencies (a) ω_r and (b) ω_r with those obtained from analytical approximation (19) and corresponding ω_r as functions of k and v_{th} . Markers at various k values represent simulation data such that the markers and curves from top to bottom correspond to $v_{th} = 0.001$ to 0.026 .

V. PHASE-MIXING SUPPLEMENTED DAMPING OF THE EMHD PERTURBATIONS

Relatively larger damping of the whistler perturbations at smaller k in comparison to the analytical estimates (10), (11) and (19) is interpreted based on the deterministic evolution of the electron distribution function governed by the Vlasov equation as simulated and analyzed in this section. In warm electron plasmas the initial damping is found to have considerable contribution from the corresponding deterministic phase-mixing process of the fresh (initial) perturbations made to the plasma, confirming to a propagating whistler wave. Note that the term *phase-mixing* used here refers to the varied response of the electrons of different velocities (from a wider spread about mean) to the propagating wave perturbation. The deterministic deformations of the velocity distribution function that evolve antisymmetrically about a reference velocity (distinct for electrostatic and electromagnetic waves) in the phase-space however introduce incoherence between the substructures of observable macroscopic spatio-temporal variations, or collective wave perturbations. The resultant weakening of the per-

turbations translates in to an additional damping (than what caused by the resonant electrons) detectable in the deterministic Vlasov simulation data. At shorter time scales this contribution supplements, and modifies, the damping of the (transverse) wave, producing enhanced damping rates in comparison to the pure resonant damping essentially estimated considering the long time limit [9]. Clear signatures of both resonant and non resonant processes are visible in the simulated 3-dimensional electron velocity distribution function evolving in the phase-space.

A. Phase-space evolution of whistler wave perturbation in the Vlasov simulations

The plots of electron distribution function perturbation $f_1 = f - f_0$, as available from the simulations done with denser grid size, $64 \times 160 \times 160 \times 160$, are analyzed in order to understand the kinetics of the evolution of whistler wave perturbation in the plasma. Since the system is periodic and transverse, analyzing the f data from any chosen spatial location is equivalent. The location $z = L/2$, or the center of the simulation domain, is therefore chosen here as the representative location in the simulation domain. For added accuracy, both f and f_0 are evolved under equivalent Vlasov simulation operation in order to obtain $f_1(t)$ presented below. From the full 3-dimensional velocity distribution function available, the evolution of $f_1(z = L/2, v_z, v_x, v_y)$ at various stages of time is presented in Fig. 7 from the cold electron case simulation, performed with sufficiently small T_e such that the $|v_{res}| \gg v_{th} = 0.001 c$. Because of the small electron temperature, both the resonant and phase velocity of the whistler are far removed from the distribution width (along $v_z \parallel \mathbf{k}$) and the f_1 plotted in three columns of frames from left to right correspond to velocity values $v_z = -v_{th}, 0$ and v_{th} , respectively. The same data is plotted in Fig. 8 from simulation of warmer electrons case, $|v_{res}| \leq v_{th} = 0.001 c$, such that sufficient population of resonant electrons is present with $v_z = v_{res}$, producing dominant and analyzable kinetic effects. The rows of frames from top to bottom in both plots correspond to time from $t = 0$ to $20 \omega_{pe}^{-1} (\equiv 2\Omega_{ce}^{-1})$.

In both cold and warm electron cases plotted in top rows of Fig. 7 and Fig. 8, respectively, the f_1 plotted at $t = 0$, consistent with a whistler phase-space perturbation in the velocity space, has a nonzero velocity perturbation purely aligned to \hat{v}_y . The following rows cover evolution over a period of $20\omega_{pe}^{-1}$, or one complete whistler cycle. We first discuss evolution of perturbation in the cold electron case presented in Fig. 7. Consider the evolution of the perturbation component located at $v_z \sim 0$ plotted in the second column of the Fig. 7. Because of being drawn from vanishing v_z , this component of f_1 does not have electrons that leave to, or arrive from, the adjacent z locations as the time progresses (i.e., from top frame to bottom frame). Therefore, the participating

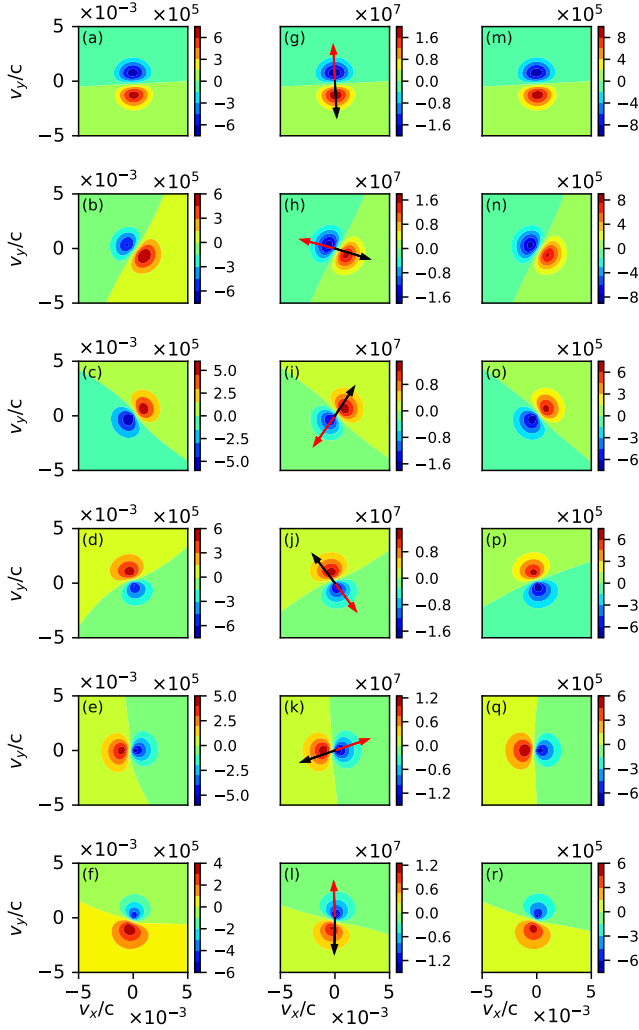


FIG. 7. Evolution of the electrons velocity distribution function perturbation in the transverse velocity-space plane v_x - v_y for the cold electrons case, with $v_{th} = 0.001c$. Frames from top to bottom correspond to equal intervals over one whistler cycle ($\sim 20\omega_{pe}^{-1}$) from $t = 0$, while those from left to right are for $v_z = -v_{th}$, 0, and v_{th} , respectively. Red and black arrows indicate, \mathbf{B}_1 and $\langle \mathbf{v} \rangle_1$, respectively.

electrons are simply displaced to newer angular locations with (angular) velocity Ω_{ce} on the same transverse velocity plane v_x - v_y in the subsequent frames, with respect to their original locations in the $t = 0$ frame. However the polarization of the perturbation in this case rotates with angular velocity of the wave ω , dissimilar to Ω_{ce} ($> \omega$, the reason for which is well encoded in the linear theory of waves in magnetized plasmas). Drawn from the simulation data for $\langle \mathbf{v} \rangle_1$ and \mathbf{B} , the black and red arrows represent phases of right handed polarized velocity and magnetic field vectors, respectively, for the reference. The rotation in perturbation polarization consistent with wave frequency confirms that the initial perturbation efficiently excited a whistler eigenmode in the simulated

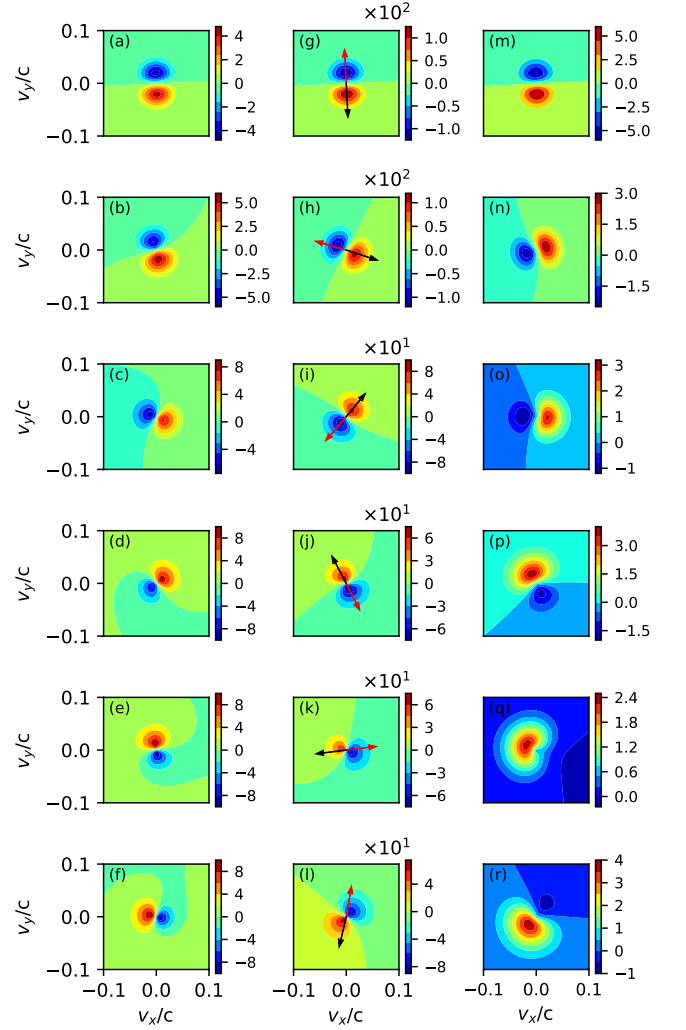


FIG. 8. Evolution of the electrons velocity distribution function perturbation in the transverse velocity-space plane v_x - v_y for the warm electrons case, with $v_{th} = 0.02c$. Frames from top to bottom correspond to equal intervals over one whistler cycle ($\sim 20\omega_{pe}^{-1}$) from $t = 0$, while those from left to right are for $v_z = v_{res}$, 0, and v_{phase} , respectively. Red and black arrows indicate, \mathbf{B}_1 and $\langle \mathbf{v} \rangle_1$, respectively.

magnetized plasma right from $t = 0$.

The kinetic effects because of resonant electrons are addressed further below in warm electron case since for cold electrons the velocity distribution drops to negligible values at the resonant velocity. The same is evident from the identical evolution of the perturbation component at $v_z = |\pm v_{th}| \ll |v_{res}|$, plotted in the columns 1 and 3, respectively, which show rotation of perturbation polarization with same frequency and a coherent response of electrons of all v_z values due to the distribution function being nearly a delta function in velocities both along and across \mathbf{k} . Therefore, the fluid theory results ($\gamma \rightarrow 0$, ω given by (18)) remain suitably recoverable for this cold electron case as clear from the data point corresponding

to $v_{th} \sim 0.001c$ in Fig. 4.

We now show that an identical initial perturbation, that excited a nearly ideal whistler eigenmode in the above cold electron case, evolves in a warm electron magnetized plasma exhibiting a far richer kinetic response. This initial evolution, covering $20\omega_{pe}^{-1}$ remains applicable, for example, to the short lived transverse whistler mode fluctuations characteristically running much of weak electromagnetic plasma turbulence [3]. There evolution therefore necessitates invoking initial phase-mixing description of analytical kinetic theory results in addition to the routine estimates of damping by pure resonant electrons.

Considering the evolution for the perturbation component at $v_z \sim 0, z = L/2$ plotted in the middle column of the frames in Fig. 8 we note that its polarization rotates nearly with the wave frequency ω , however with a visible shortfall in comparison to the cold electron case. The electrons being sufficiently warm in this case, it is now possible to examine the f_1 evolution at the resonant velocity for this set of data, which is noted to be much distinct as plotted in the first column of the Fig. 8.

Note that individual electrons streaming with resonant velocity v_z would see the wave frequency Doppler-shifted to Ω_{ce} and therefore will be perpetually accelerated by the wave \mathbf{E}_1 in transverse the direction. The resulting proliferation of electrons to higher v_\perp is visible with time in frames from (a)-(f). It is important to notice, though, that, unlike the coherent response of the full distribution in cold electron case, the polarization of the perturbation in the resonant electrons has rotated with a considerably lower frequency, thereby covering a lesser angle as compared to the bulk, or $v_z \sim 0$, electrons.

Quantitative estimation of this shift in frequency is possible based on the fact that because of $\Omega_{ce} > \omega$, in time δt the gyrating electrons cover a far larger angle in the transverse plane than the rotating polarization of the perturbation. Consequently, as the time progresses the $v_z = v_{res}$ electrons bring imprint of an increasingly older phase of the wave, distinct from the instant phase of the bulk electron component polarization (seen in the corresponding middle column frame plotted for $v_z = 0$). This is despite of resonant electrons arriving (because of their negative streaming velocity $v_{res} < 0$) from a forward location $z = \delta z > L/2$ having a slightly advanced phase of the wave.

The convected phase $\phi(z = L/2, t = \delta t)$ of the polarization for resonant perturbation component (perturbation component with $v_z = v_{res}$) at time $t = \delta t$ can be calculated by using a transformation between present and older phase of the polarization of the perturbation,

$$\phi(L/2, \delta t) = \phi(L/2 + \delta z, 0) = \phi_0 + \delta\phi_z + \delta\phi_\theta, \quad (20)$$

where ϕ_0 is instant phase of the polarization of the bulk perturbation at $z = L/2$ (as visible in $v_z = 0, t = \delta t$ frame), $\phi(z, t)$ is the general phase of the polarization (ideally known from the cold electron limit), $\delta\phi_z$ and $\delta\phi_\theta$ are the phase difference arising from change in z and

θ , respectively. For the resonant component of the perturbation, we have,

$$\delta\phi_z = \delta z k = v_{res}(-\delta t)k; \quad \delta\phi_\theta = (-\delta t) \Omega_{ce}. \quad (21)$$

Since $v_{res} < 0$ and $\Omega_{ce} > \omega = \Omega_{ce} - |v_{res}|k$, we have $\delta\phi_z > 0, \delta\phi_\theta < 0$ and $|\delta\phi_\theta| > \delta\phi_z$, meaning that the phase of resonant component of the perturbation relative to instant bulk electron phase will be negative. These phase delays are in excellent agreement with the phase difference in the frames presenting the resonant component of the perturbation in the first column of Fig. 8.

An even distinct evolution is witnessed in the perturbation component at the positive values of parallel velocity, $v_z > 0$, as potted in third column of Fig. 8 for $v_z = v_{phase}$. Before explanation of this behavior, which strongly relates to phase-mixing process of the whistler perturbation, it can be clearly noted that the strength of macroscopic wave variables (especially \mathbf{J}_1) is going to be weakened with time if velocity integration is performed at advanced times using $f_1(v_x, v_y)$ that has its peaks in v_x - v_y plane initially overlapping for all v_z , but dispersed, at future times, over a wider range of angles for different v_z .

In the f_1 evolution plotted at $v_z = v_{phase}$ in third column of Fig. 8, the streaming (and simultaneously gyrating) electrons experience the wave fields purely non-rotating. At each δt they import, from their original locations to $z = L/2$, the phase as determined by the transformation (20). In this case, however, with each gyration completed, the electrons additionally drift orthogonal to the phase of the wave electric field experienced by them. Consequently, the imported f_1 is additionally displaced away from $v_\perp = 0$. With time progressing, the f_1 steadily sampled at $z = L/2$ witnesses newer electrons arriving from backward locations. An increasing drift is therefore witnessed in f_1 , rotated at an incremented angle in v_x - v_y plane. This results in periodically separating red and blue patches, absent initially. Note that the initial transverse velocity perturbation at $t = 0$ is introduced with no such nonuniformity with respect to v_z . This nonuniformity clearly develops over the time-scale of an electron gyroperiod.

B. Kinetic model for initial-value transverse electromagnetic perturbations

Out of the several kinetic modifications of f_1 witnessed above, those attributable to the wave fields and those to ballistic effects can be distinguished and analyzed based on the linearized Laplace-Fourier transformed Vlasov-Maxwell system of equations,

$$\begin{aligned} (p + i\mathbf{k} \cdot \mathbf{v})f_{kp1}(\mathbf{v}) &= f_{k1}(t=0) \\ &+ \frac{e}{m_e} \left(\frac{\mathbf{v} \times \mathbf{B}_0}{c} \right) \cdot \nabla_v f_{kp1}(\mathbf{v}) \\ &+ \frac{e}{m_e} \left(\mathbf{E}_{kp1} + \frac{\mathbf{v} \times \mathbf{B}_{kp1}}{c} \right) \cdot \nabla_v f_0(\mathbf{v}) \end{aligned} \quad (22)$$

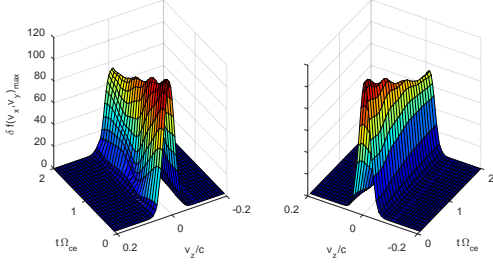


FIG. 9. Time evolution of the maximum amplitude, $f_{1\max}$, of electrons velocity distribution function perturbation $f_1(v_x, v_y)$ plotted in Figs. 7 and 8 in full range of v_z , for the hot electrons case ($v_{th} = 0.02c$). Plots (a) and (b) present relatively rotated views of the same surface for clearer exposure of the both sides about the surface maximum.

$$\mathbf{B}_{kp1} = \mathbf{B}_{k1}(t=0) + \frac{c}{ip}(\mathbf{k} \times \mathbf{E}_{kp1}). \quad (23)$$

and

$$\mathbf{E}_{kp1} = \mathbf{E}_{k1}(t=0) - \frac{c}{ip} \left(\mathbf{k} \times \mathbf{B}_{kp1} - \frac{4\pi}{c} \mathbf{j}_{kp1} \right), \quad (24)$$

where $p = -i\omega_r + \omega_i$ and \mathbf{E}_{kp1} and \mathbf{B}_{kp1} are the transformed wave electric and magnetic fields, respectively.

Using the well known identity for conjugate components of the velocity variable, $v_x = v_\perp \cos \phi$ and $v_y = v_\perp \sin \phi$,

$$\frac{\partial f_{pk1}(\mathbf{v})}{\partial \phi} = \left(-v_y \frac{\partial}{\partial v_x} + v_x \frac{\partial}{\partial v_y} \right) = -(\mathbf{v} \times \hat{\mathbf{z}}) \cdot \nabla_v f_{pk1}(\mathbf{v}),$$

Eq. (22) can be rewritten as,

$$\begin{aligned} \frac{(p + i\mathbf{k} \cdot \mathbf{v})}{\Omega_{ce}} f_{kp1}(\mathbf{v}) + \frac{\partial f_{pk1}(\mathbf{v})}{\partial \phi} &= \frac{f_{k1}(t=0)}{\Omega_{ce}} \\ &+ \frac{e}{m_e \Omega_{ce}} \left(\mathbf{E}_{kp1} + \frac{\mathbf{v} \times \mathbf{B}_{kp1}}{c} \right) \cdot \nabla_v f_0(\mathbf{v}). \end{aligned} \quad (25)$$

Note that the wave field generated v_z specific modifications, including (i) the acceleration of resonant electrons and (ii) the slowly building electron drift for $v_z \sim v_{\text{phase}}$, can be resolved, approximately, from the fundamentally kinetic ballistic modifications in the f_1 at shorter times ($\Omega_{ce}^{-1} < t < \omega^{-1}$) when the latter dominate the former. In order to do this, we first write the right handed polarized component of the Vlasov equation [26] applicable to the whistler mode,

$$\begin{aligned} \frac{d}{d\phi} \left\{ f_{1+}(\mathbf{v}) \exp \left[\frac{(p + ikv_z)}{\Omega_{ce}} \phi \right] \right\} &= \\ \frac{f_{k1+}(t=0)}{\Omega_{ce}} \exp \left[\frac{(p + ikv_z)}{\Omega_{ce}} \phi + i\phi \right] & \\ + F_+(v_z, v_\perp) \exp \left[\frac{(p + ikv_z)}{\Omega_{ce}} \phi + i\phi \right] & \end{aligned} \quad (26)$$

where $v_\perp = (v_x^2 + v_y^2)^{\frac{1}{2}}$, f_{k1+} is right handed circularly polarized part of the initial perturbation. The quantity

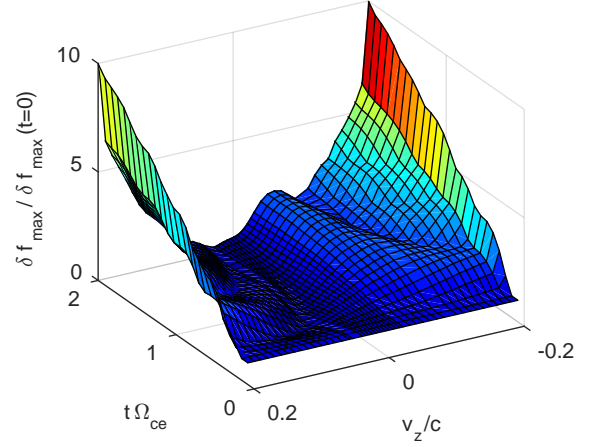


FIG. 10. Surface in the figure normalized to individual initial values at each v_z .

$F_+(v_z, v_\perp)$ is obtained by ignoring $\mathbf{B}_k(t=0)$ in Eq. (23), as,

$$F_+(v_z, v_\perp) = \frac{e}{m_e \Omega_{ce}} \left[\left(1 - \frac{kv_z}{\omega} \right) \frac{\partial f_0}{\partial v_\perp} + \frac{kv_z}{\omega} \frac{\partial f_0}{\partial v_\perp} \right] \frac{E_+}{\sqrt{2}} \quad (27)$$

where $E_+ = E_x - iE_y$. Both sides of Eq. (26) can be integrated with respect to ϕ from $\phi = -\infty$ to instant ϕ by assuming very small imaginary part in ω , yielding the time asymptotic solution,

$$\begin{aligned} f_{pk1+}(\mathbf{v}) &= \frac{f_{k1+}(t=0)e^{i\phi}}{(p + ikv_z + i\Omega_{ce})} \\ &+ \frac{\Omega_{ce}}{(p + ikv_z + i\Omega_{ce})} F_+(v_z, v_\perp) e^{i\phi}. \end{aligned} \quad (28)$$

This means that all the right handed circularly polarized transverse modes are obtainable by accounting for the poles of the second term, which represents the contribution of the electric and magnetic fields of the wave. For example, the Whistler mode corresponds to E_+ obtained in terms of B_+ and J_+ using (22)-(24) in the limit $\Omega_{pi} < \omega < \Omega_{ce}$ such that the relevant pole appears where the dispersion function for an isotropic electron distribution,

$$c^2 k^2 - \omega^2 - \frac{8\pi^2 q_e^2}{m} \int_{-\infty}^{\infty} \int_0^{\infty} \frac{[(\omega - kv_z + kv_\perp) \frac{\partial f_{e0}}{\partial v_z}]}{(\omega - kv_z \pm \Omega_{ce})} \times v_\perp^2 dv_\perp dv_z \quad (29)$$

vanishes, yielding both ω_r and γ [8]. However, the solution (28) indicates that $f_{pk1+}(\mathbf{v})$, being the integrand of the Landau-like Laplace inversion integral producing $f_{k1+}(\mathbf{v}, t)$ (which can, in turn, be compared to the simulation outputs plotted in Fig. 7 and 8), has an additional pole at,

$$p = -i(kv_z + \Omega_{ce}). \quad (30)$$

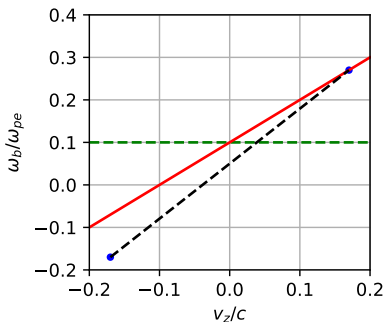


FIG. 11. The simulated v_z dependence frequency ω_b (dotted line, circular markers) estimated from the Fig. 10 compared with analytical expression (30) (solid line) for frequency of amplitude oscillation resulting from phase-mixing.

Since k , v_z and Ω_{ce} are real, there is no reduction expected with time in the amplitude of perturbation components corresponding to various v_z . Instead, $f_{k1+}(v_z, t)$ must develop temporal oscillations with a pure real frequency $\omega_b(v_z)$ directly proportional to v_z . As seen below, this temporal modulation is caused by the information of the wave phases at remote locations being brought by the electrons at the location of measurement, at different temporal rates for different v_z .

The net (kinetic) reduction in the wave strength is therefore caused by both, (i) a phase-mixing process present throughout the velocity space and (ii) the resonant damping which is dominant at the resonant velocity, accelerating only the resonant electrons. While both these processes in a collisionless warm plasma conserve the entropy despite diminishing the wave strength [9], only the latter contributes to the routinely estimated γ . The temporal damping caused by former involves pure frequencies and cause a rather *deterministic thermalization* (reversible or entropy preserving ergodization), or a *phase-mixing*, of the transverse distribution (and, consequently of \mathbf{J}_+). As presented below, this phase-mixing is clearly recoverable from the output of a deterministic simulation performed in this study, duly described by the above analytical treatment.

The maxima of $f_1(v_x, v_y)$ presented in Fig. 8, corresponding to hot electron case, are plotted separately as a function of v_z and t in the form of the surface $f_{1\max}(v_z, t)$ in Fig. 9. For the convenience, two views of the surface are presented in (a) and (b) with relative rotation to clearly highlight the visible temporal variation of f_{\max} at various v_z , including $v_z = v_{\text{res}}$ as indicated by an arrow. The perturbation amplitude in Fig. 9 shows that only at $v_z = v_{\text{res}}$ a nearly monotonic variation is present in the amplitude, whereas at velocities away from v_{res} a slow temporal oscillation enters in the amplitude of f_1 with its frequency increasing with $|v_z|$. The high frequency oscillations in small v_z region are remnants of high frequency ($\omega_{R,L} > \Omega_{ce}$) RHCP and LHCP waves (see Fig. 3) and should not be confused with the discussed low frequency high amplitude oscillations in the small v_z region.

This additional frequency in the surface plot contours for larger v_z (> 0) results from the streaming electrons importing information of polarization from adjacent locations based on the transformation Eq. (20). Note that because of the periodic set up, for a larger velocity, say $v_z \sim n(k\delta t)^{-1}$, the information being imported would contain n cycles of modulation, corresponding to n consecutive spatial periods sampled by fast streaming electrons in the time interval δt past $t = 0$. The frequency of temporal modulation in $f_{1\max}(v_z, t)$ therefore must increase with v_z value being examined at a fixed location $z = L/2$. This dependence on v_z is indeed confirmed by plotting, in Fig. 10, the amplitude $f_{1\max}(v_z, t)$ normalized to its $t = 0$ reference value for each v_z , such that the modulations become clearly identifiable even at the larger v_z where the distribution function f_0 as well as the amplitude of f_1 drop to significantly small values.

The perturbation information at $z = L/2$ arriving loaded on electrons streaming with phase velocity is played faster than the rotation of bulk polarization (as $\omega < \Omega_{ce}$) but imports an increasingly delayed phase (causing the rotation appearing to stop or reversed over certain intervals). Additionally, after certain time interval, it begins to display the signatures of freshly developed $\mathbf{E}_1 \times \mathbf{B}_0$ drift.

Finally, since electrons with $v_z > v_{\text{res}}$ are effectively magnetized to a higher degree on the wave time scale experienced by them, $(\omega - kv_z)^{-1} \gg \Omega_{ce}^{-1}$, they participate rather efficiently in the collective wave propagation. However, a Doppler down-shifted frequency experienced, and responded to, by this majority of electrons causes the wave collective ω_r to reduce in accordance with dispersion (17). This reduction in ω_r is duly captured by the present Vlasov simulation results, as clear by comparing Fig. 7 with Fig. 8.

VI. SUMMARY AND CONCLUSIONS

The kinetic damping mechanism of low frequency transverse perturbation propagating parallel to the magnetic field in a magnetized warm plasma is simulated by means of Vlasov simulations. The impact of finite temperature on the wave frequency and the underlying physics of the analytical approximations prescribing reduction in the real frequency of the wave in a warm plasma is addressed and resolved by full 4D phase-spatiotemporal evolution simulated of the electron distribution function.

The analysis of the Vlasov simulation output illustrates and estimates the evolution of initially coherent perturbations that undergo damping by mutually separable initial kinetic evolution operating over the global and local regions of the of electron velocity space. The net kinetic effects contributed reduction in the strength of perturbations is caused by both, (i) a phase-mixing process present throughout the velocity space and (ii) the resonant damping which is dominant at the resonant velocity,

accelerating only the resonant electrons. The quantitative analysis of the amplitude oscillation produced by the former is done and their interplay, at short times, with the modifications of the initial perturbations by the resonant electrons is shown to result in enhanced decay of the perturbation amplitude as compared to typical long time estimates of the damping. It is emphasized that while both these mechanisms in a collisionless warm plasma conserve the entropy, it is only the resonant effects that contributes to the routinely estimated damping rate γ . The analytically predicted reduction in the real wave frequency ω_r is duly recovered by the simulations. This is shown to follow from a greater effective magnetization of dominant $v_z > v_{\text{res}}$ electron population, which, how-

ever, experiences frequency of the wave Doppler-shifted to smaller values.

We conclude by discussing that access to rather self-consistent analytical initial value solutions of the problem (22)-(24) remain of high relevance. They should enable the output from the present fully kinetic electromagnetic transverse wave Vlasov simulations to more carefully determine, for example, the spectral boundaries of the electromagnetic collisionless plasma turbulence. The associated particle and energy transport in the space and fusion plasma, in turn, can also be approached more deterministically.

Acknowledgement: The simulations are performed on the IPR HPC supercomputing cluster ANTYA.

-
- [1] J. E. Borovsky, *Journal of Geophysical Research* **117**, 5104 (2012).
 - [2] J. J. Podesta, D. A. Roberts, and M. L. Goldstein, *The Astrophysical Journal* **664**, 543 (2007).
 - [3] S. P. Gary, S. Saito, and Y. Narita, *The Astrophysical Journal* **716**, 1332 (2010).
 - [4] X. Xu, L. Chen, C. Zhou, X. Liu, Z. Xia, J. J. Simpson, and Y. Zhang, *Journal of Geophysical Research: Space Physics* **125**, e2019JA027750 (2017).
 - [5] R. A. Helliwell, *Whistlers and related ionospheric phenomena* (Press, Stanford, Calif: Stanford Univ., 1965).
 - [6] F. Xiao, S. Liu, X. Tao, Z. Su, Q. Zhou, C. Yang, Z. He, Y. He, Z. Gao, D. N. Baker, H. E. Spence, G. D. Reeves, H. O. Funsten, and J. B. Blake, *Journal of Geophysical Research: Space Physics* **122**, 3201–3211 (2017).
 - [7] R. M. Thorne, *Geophys. Res. Lett.* **37**, L22107 (2010).
 - [8] L. Chen, R. M. Thorne, Y. Shprits, and B. Ni, *Journal of Geophysical Research: Space Physics* **118**, 2185 (2013).
 - [9] N. A. Krall and A. W. Trivelpiece, *Principles of Plasma Physics* (San Francisco Press Inc., San Francisco, 1986).
 - [10] L. D. Landau, *C. R. Acad. Sci. U. R. S. S.* **44**, 311 (1944).
 - [11] L. D. Landau, *J. Phys. U.S.S.R.* **10**, 25 (1946).
 - [12] R. Lutomirski, *The Physics of Fluids* **13**, 149 (1970).
 - [13] E. Fijalkow, *Computer physics communications* **116**, 329 (1999).
 - [14] A. Mangeney, F. Califano, C. Cavazzonic, and P. Travnicek, *Journal of Computational Physics* **179**, 495 (2002).
 - [15] L. Palodhi, F. Califano, and F. Pegoraro, *Plasma Physics and Controlled Fusion* **52**, 095007 (2010).
 - [16] F. Valentini, P. Travnicek, F. Califano, P. Hellinger, and A. Mangeney, *Journal of Computational Physics* **225**, 753 (2007).
 - [17] J. R. Shuster, N. Bessho, S. Wang, and J. Ng, *Physics of Plasmas* **28**, 122902 (2021).
 - [18] T. Fülöp, H. Smith, and G. Pokol, *Physics of Plasmas* **16**, 022502 (2009).
 - [19] C. Schreiner, P. Kilian, and F. Spanier, *Communications in Computational Physics* **21**, 947 (2017).
 - [20] C. Schreiner, *Numerical modelling of the microphysical foundation of astrophysical particle acceleration*, Ph.D. thesis, North-West University (South Africa), Potchefstroom Campus (2016).
 - [21] D. Mandal and D. Sharma, *Journal of Physics: Conference Series* **759**, 012068 (2016).
 - [22] D. Mandal, D. Sharma, and H. Schamel, *Phys. Plasmas* **27**, 022102 (2020).
 - [23] S. P. Gary, *Theory of space plasma microinstabilities*, 7 (Cambridge university press, 1993).
 - [24] F. F. Chen, *Introduction to Plasma Physics* (Springer Science & Business Media, 2012).
 - [25] T. H. Stix, *Waves in plasmas* (Springer Science & Business Media, 1992).
 - [26] J. A. Bittencourt, *Fundamentals of plasma physics* (Springer Science & Business Media, 2013).
 - [27] M. Abramowitz and I. A. Stegun, *Handbook of Mathematical Functions with Formulas, Graphs, and Mathematical Tables*, ninth dover printing, tenth gpo printing ed. (Dover, New York, 1964).